JOURNAL OF GEOPHYSICAL RESEARCH, VOL. 115, C04010, doi:10.1029/2009JC005647, 2010

Intraseasonal variability in sea surface height over the South China Sea

Wei Zhuang,[1] Shang-Ping Xie,[2] Dongxiao Wang,[1] Bunmei Taguchi,[3] Hidenori Aiki,[3] and Hideharu Sasaki[3]

Received 16 July 2009; revised 1 November 2009; accepted 11 November 2009; published 7 April 2010.

[1] Intraseasonal sea surface height (SSH) variability and associated eddy energy in the South China Sea is studied using satellite observations and an eddy-resolving, global ocean general circulation model. In both the model hindcast and satellite observations, a conspicuous minimum of intraseasonal SSH variance is found along the continental break between the shallow shelf and deep basin. Specifically strong intraseasonal variability (ISV) exists in the following regions: on the northern continental shelf, in the Gulf of Thailand, and along two bands in the deep basin with the northern band located west of Luzon Strait and the southern one southeast of Vietnam. SSH ISV exhibits clear seasonality. During active seasons, ISV in the deep water, high-variance bands displays robust propagations in the direction of mean flow. Low correlation between observations and model hindcast suggests the importance dynamical instabilities for ISV in the deep basin, in agreement with an energetics analysis. An exception is along the Vietnam offshore jet during summer, where ISV is forced by wind curls created by Annam Cordillera. In shallow waters, especially in the Gulf of Thailand, SSH ISV is dominated by barotropic response to intraseasonal wind stress forcing. The agreement between altimetry and the model simulation in the Gulf of Thailand demonstrates the ability of satellite altimeters to observe SSH variability in shallow shelves of weak tides.

Citation: Zhuang, W., S.-P. Xie, D. Wang, B. Taguchi, H. Aiki, and H. Sasaki (2010), Intraseasonal variability in sea surface height over the South China Sea, *J. Geophys. Res.*, *115*, C04010, doi:10.1029/2009JC005647.

1. Introduction

[2] The South China Sea (SCS) is a large semienclosed marginal sea located between the western Pacific Ocean and eastern Indian Ocean, covering an area from 3°S to 23°N and from 99°E to 121°E. It is connected with the East China Sea to the northeast (via Taiwan Strait), the Pacific Ocean and the Sulu Sea to the east (via Luzon and Mindoro Straits, respectively), the Java Sea to the south (via Karimata Stait) and the Indian Ocean to the west (via Malacca Strait). All of these straits are shallow except the Luzon Strait, which features a sill deeper than 2000 m. The bathymetry of the SCS is complex with a deep basin in the center elongating in the northeast-southwest direction (Figure 1b). The main shallow regions include the Gulf of Thailand and the Sunda Shelf in the southwest, the northern SCS (NSCS) shelf along the Chinese and northern Vietnam coasts.

[1]Key Laboratory of Tropical Marine Environmental Dynamics, South China Sea Institute of Oceanology, Chinese Academy of Sciences, Guangzhou, China.
[2]International Pacific Research Center and Department of Meteorology, University of Hawai'i at Manoa, Honolulu, Hawaii, USA.
[3]Earth Simulator Center, Japan Agency for Marine-Earth Science and Technology, Yokohama, Japan.

0148-0227/10/2009JC005647

[3] Sea surface height (SSH) is a useful indicator of upper ocean circulation. There is a long history of studying SCS surface circulation. Pioneering works note a distinct seasonal cycle of basin-scale circulation, predominantly cyclonic in winter and anticyclonic in summer [*Dale*, 1956; *Wyrtki*, 1961] with stationary eddies embedded [*Xu et al.*, 1982]. The seasonal cycle in SSH is forced mainly by the monsoon through baroclinic Rossby waves [*Z. Liu et al.*, 2001; *Gan et al.*, 2006]. In the NSCS, the circulation is influenced by the Kuroshio intrusion [*Shaw*, 1991; *Qu*, 2000], for which mesoscale eddies appear important [*Yuan et al.*, 2006].

[4] Satellite altimeter observations have revealed rich SSH variability on the mesoscale [*Shaw et al.*, 1999; *Ho et al.*, 2000a] and interannual timescales [*Ho et al.*, 2000b; *Hwang and Chen*, 2000]. Interannual variability in SSH and sea surface temperature (SST) is highly correlated with El Niño and Southern Oscillation (ENSO) [*Xie et al.*, 2003; *Liu et al.*, 2004; *Wu and Chang*, 2005; *Fang et al.*, 2006; *C. Wang et al.*, 2006]. Ocean dynamical adjustments take place on interannual timescales [*Qu et al.*, 2004; *Cheng and Qi*, 2007; *Rong et al.*, 2007], affecting SST via horizontal advection [*Xie et al.*, 2003; *Liu et al.*, 2004].

[5] The SCS monsoon displays significant intraseasonal variability (ISV) with two dominant periods of 30–60 and 10–25 days [*Lau et al.*, 1988; *Annamalai and Slingo*, 2001; *Mao and Chan*, 2005; *Kajikawa and Yasunari*, 2005]. In

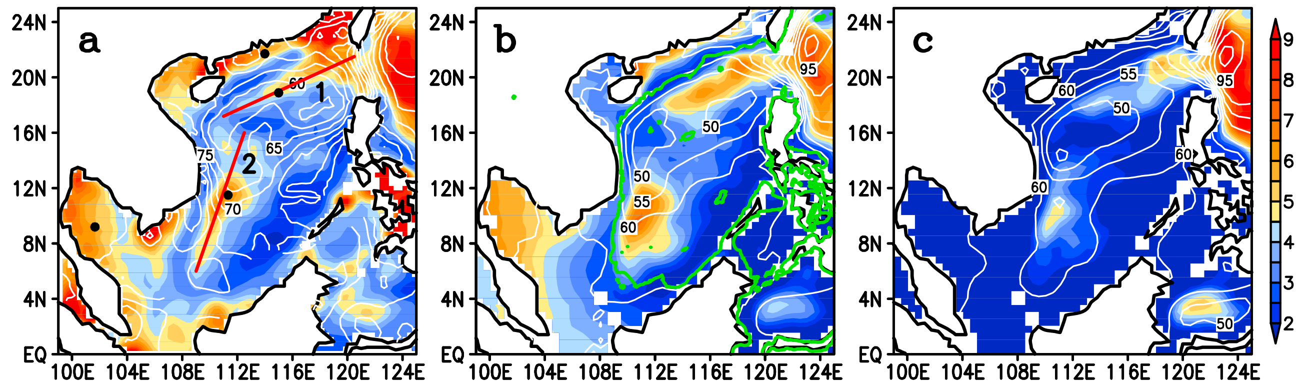

Figure 1. Annual mean standard deviation of sea level ISV (cm, shaded areas) and the mean sea surface topography (cm, white contours) for (a) observations, (b) the QSCAT, and (c) CLIM runs. Red lines in Figure 1a are along high-variance bands in the deep basin. Green contours in Figure 1b represent the 150 m isobath.

response to atmospheric forcing, SST in the SCS displays strong ISV features with distinct seasonality [*Gao and Zhou*, 2002]. In summer, SST ISV is strong off southern Vietnam associated with the ISV of an orograhic wind jet [*Xie et al.*, 2007]. Based on buoy and satellite altimeter observations, *Q. Liu et al.* [2001] note that ISV in the thermocline depth in the central SCS is greatly influenced by mesoscale eddies and is out of phase with the SSH. ISV in subsurface temperature also exists in the NSCS, associated with westward propagating mesoscale eddies that originate near the Luzon Strait [*Wu and Chiang*, 2007]. Some in situ current measurements near the southern tip of Taiwan Island reveal significant ISV in the velocity field associated with local wind curls [*Wu et al.*, 2005].

[6] Energetic mesoscale eddies have been observed in the SCS from hydrographic data [*Chu et al.*, 1998; *Fang et al.*, 2002] and their geographical distributions are mapped from satellite altimetry [*G. Wang et al.*, 2003]. A recent numerical study by *Xiu et al.* [2010] indicates that strong eddies usually last longer and penetrate deeper than weaker ones. Based on along-track TOPEX/Poseidon (T/P) altimeter data, significant mesoscale variability in the SCS is found along two bands, along the western boundary and oriented in a southwest to northeast direction across the central SCS [*Wang et al.*, 2000]. *Metzger and Hurlburt* [2001] suggest that eddy variability in the SCS is to a large degree nondeterministic on interannual timescales.

[7] The scarcity of in situ observations prevents a detailed description of the intraseasonal SSH variability in the SCS. As for satellite observations, high-frequency (HF) variability at period shorter than 20 days could be aliased into lower frequencies and contaminate altimeter measurements. The sources of such aliasing could be tides [e.g., *Schlax and Chelton*, 1994] or HF atmospheric forcing [e.g., *Fukumori et al.*, 1998]. To mitigate aliasing errors, previous studies on SCS sea level variability tend to filter out some intraseasonal signals or directly make seasonal means [e.g., *Shaw et al.*, 1999; *Wang et al.*, 2000]. The present tidal models have reached centimetric accuracy in the deep ocean, but are still unable to remove all tidal aliasing in shallow waters [*Lyard et al.*, 2006]. The alias of atmospheric-forced HF signals can now be largely suppressed by subtracting model-simulated HF variability [*Carrère and Lyard*, 2003]. Compared with previous altimetry products, the newly released altimetry data set (since 2005) makes better tidal and atmospheric barometric correction. The improved accuracy enables the study of sea level variability even over some continental shelves [*Volkov et al.*, 2007].

[8] The present study systematically maps the spatial and seasonal variations in sea level ISV over the SCS, and explores their dynamics. We take advantage of the upgraded altimetry data set, together with simulations by a global eddy-resolving model. The synergy of satellite observations and model simulations reveals bands of strong ISV over the SCS. Intraseasonal SSH variations are distinct in their dynamics between the shelf and deep basin. In shallow zones, ISV reflects wind-driven barotropic motions while it is associated with mesoscale eddy propagations in deep regions due to mean flow instabilities.

[9] The organization of this paper is as follows. Section 2 describes observational data and model output. Section 3 illustrates the spatial distribution of sea level ISV and its seasonality. Sharp differences between the shelf and deep basin are highlighted. Section 4 explores physical mechanisms for ISV in several parts of the SCS. Section 5 is a summary.

2. Observations and Model

2.1. Observational Data

[10] Sea level anomaly (SLA) has been measured by multisatellite altimeters for more than one decade. We adopt the merged SLA data derived from simultaneous measurements of two satellites (TOPEX/Poseidon or Jason-1 and ERS or Envisat), which are distributed by Archiving, Validation and Interpretation of Satellite Oceanographic data (AVISO). The estimation of mesoscale signals is greatly improved from one to two satellites [*Le Traon and Dibarboure*, 1999]. In 2005, the multimission altimeter data set is updated with new corrections using a new tidal model (GOT2000, Goddard/Grenoble Ocean Tide) and a barotropic model (MOG2D-G, Modèle aux Ondes de Gravité 2-Dimensions Global) to reduce the HF aliasing [*Volkov et al.*, 2007; *Dibarboure et al.*, 2008]. The product is available on 1/3° Mercator grids, with

the meridional grid spacing kept the same as the zonal one varying from 37 km at the equator to 18.5 km at 60°N/S. The weekly mean data from 2000 to 2006 are analyzed for comparison with the OGCM simulations.

[11] We use an improved global mean dynamic topography for the annual mean, calculated from a combined analysis of drifter, satellite altimetry and wind data based on a momentum balance requirement [*Maximenko and Niiler*, 2005]. Surface wind is an important forcing for ocean circulation and SSH. The QuikScat microwave scatterometer was launched in June 1999 and measures surface wind velocity at high resolution and accuracy [*Liu*, 2002], covering 92% of the global, ice-free oceans every day. We use a product of Remote Sensing System (RSS), which maps the original swath data to a daily 0.25° × 0.25° grid.

2.2. Eddy-Resolving Model

[12] We analyze the results from an eddy-resolving OGCM for the Earth Simulator (OFES [*Masumoto et al.*, 2004; *Sasaki et al.*, 2004]). The model is based on the Modular Ocean Model (MOM3 [*Pacanowski and Griffies*, 2000]), with a near-global domain extending from 75°S to 75°N. Horizontal resolution is 0.1° × 0.1°. There are 54 vertical levels, with varying resolutions from 5 m at the surface to 330 m at the maximum depth of 6065 m.

[13] Initialized at rest with annual mean temperature and salinity fields of the World Ocean Atlas 1998 (WOA98 [*Boyer and Levitus*, 1997]), the model is spun up for 50 years with monthly climatological forcing of wind stress, heat and fresh water fluxes derived from the National Centers for Environmental Prediction/National Center for Atmospheric Research (NCEP/NCAR) reanalysis [*Kalnay et al.* 1996] for 1950–1999. Sea surface salinity (SSS) is restored to the observed monthly climatology of WOA98 [*Boyer and Levitus*, 1997]. The weekly output in the final 5 years (46–50) of this climatological (CLIM) run is used for analysis.

[14] Following the spin-up integration, a hindcast simulation from 1950 to 2005 is conducted with daily atmospheric forcing of the NCEP/NCAR reanalysis (NCEP run hereafter). The salinity fluxes are evaporation and precipitation from the daily NCEP/NCAR reanalysis with an additional SSS restoring to the WOA98 climatology [*Boyer and Levitus*, 1997]. Another hindcast run starts from the NCEP run on 20 July 1999 but is forced by daily mean surface wind stress from QuikScat measurements (QSCAT run). Other atmospheric forcing is the same as in the NCEP run [*Sasaki and Nonaka*, 2006]. This study mainly uses the QSCAT run, whose performance, as will be seen, is better than the NCEP run because of high resolution and accuracy of the wind product. The simulated fields during 2000–2006 are saved every 3 days for analysis.

[15] To extract intraseasonal/subseasonal variability, we use a 100 day high-pass filter, which is commonly used in ISV studies. For the 3 day model output and daily QuikScat wind product, an additional running mean is applied to suppress synoptic disturbances with periods shorter than 9 days. The weekly altimetric data could not resolve the sea level signals shorter than the Nyquist period of 14 days. As a result, the possible influence of significant 10–25 day monsoon ISV is partly suppressed, which, as suggested by the OFES simulation, has little effect on deep basin variability but leads to a 20% reduction in SSH ISV in shallow regions.

3. Features of Intraseasonal SSH Variability

[16] Figure 1 compares the observed and simulated annual mean SSH fields. The annual mean dynamic topography exhibits a cyclonic circulation pattern centered in the NSCS basin, with lowest sea level at around 117°E, 18°N northwest off Luzon Island. From this minimum center, the low sea level region extends southeastward to the east of Vietnam. Such a circulation pattern is similar to the historical hydrographic analysis of *Qu* [2000]. The mean SSH in the QSCAT run (Figure 1b) generally reproduces the observed field including the minimum northwest of Luzon. The cyclonic circulation pattern in the CLIM run (Figure 1c, similar to that in the NCEP run), however, shifts too much westward, with the lowest sea level displaced to the east of Vietnamese coast.

[17] Similar agreement in basin-wide circulation is found for seasonal results between observations (Figures 2a–2d) and model simulations (Figures 2e–2h and 2i–2l). In response to the monsoon forcing, basin-wide cyclonic and anticyclonic circulations are formed in the upper layer during winter and summer, respectively. Close inspection into stationary eddies embedded in basin-scale circulation indicates that the QSCAT run (Figures 2e–2h) matches observations much better than the NCEP and CLIM runs (Figures 2i–2l). The cyclonic eddy northwest off Luzon in winter and anticyclonic eddy with an offshore jet off southern Vietnam (~11°N) in summer are well simulated in the QSCAT run but not as well reproduced in other two runs. The differences between these runs confirm that the simulation of SCS circulation is sensitive to the choice of atmospheric forcing [*Metzger*, 2003]. With higher resolution and accuracy of the wind product, the QSCAT run simulates the upper ocean flow fields better than the NCEP and CLIM runs.

3.1. Intraseasonal Variance

[18] This section presents a variance analysis to elucidate the spatial distribution of ISV. Figure 1a (shaded areas) shows the standard deviation of altimetric intraseasonal SSH variability. The ISV is weakest in the southeast SCS and strong in the following four regions: (1) the NSCS shelf, (2) the Gulf of Thailand, (3) south of the NSCS continental slope west of Luzon Strait, and (4) southeast of Vietnam. Regions 1 and 2 are shallow shelves, and regions 3 and 4 are in deep water (DW; hereafter northern and southern DW bands, respectively). A recent eddy-tracking study shows that both DW bands are of high eddy occurrence [*Xiu et al.*, 2010]. SSH ISV is also large east of the Luzon Strait associated with active eddy energy [*Qiu*, 1999] but relatively small in the Strait. The ISV minimum in the strait separates high-variance zones on both sides. All these active ISV regions are simulated in the QSCAT run (Figure 1b) with some discrepancies in magnitude from observations. Large differences are found between observations and the QSCAT simulation in Taiwan Strait and the estuary of Mekong River, possibly due to tidal aliasing in altimetry as discussed in section 3.2.

[19] In both observations and the QSCAT run, intraseasonal variance features a minimum band in the northwest and

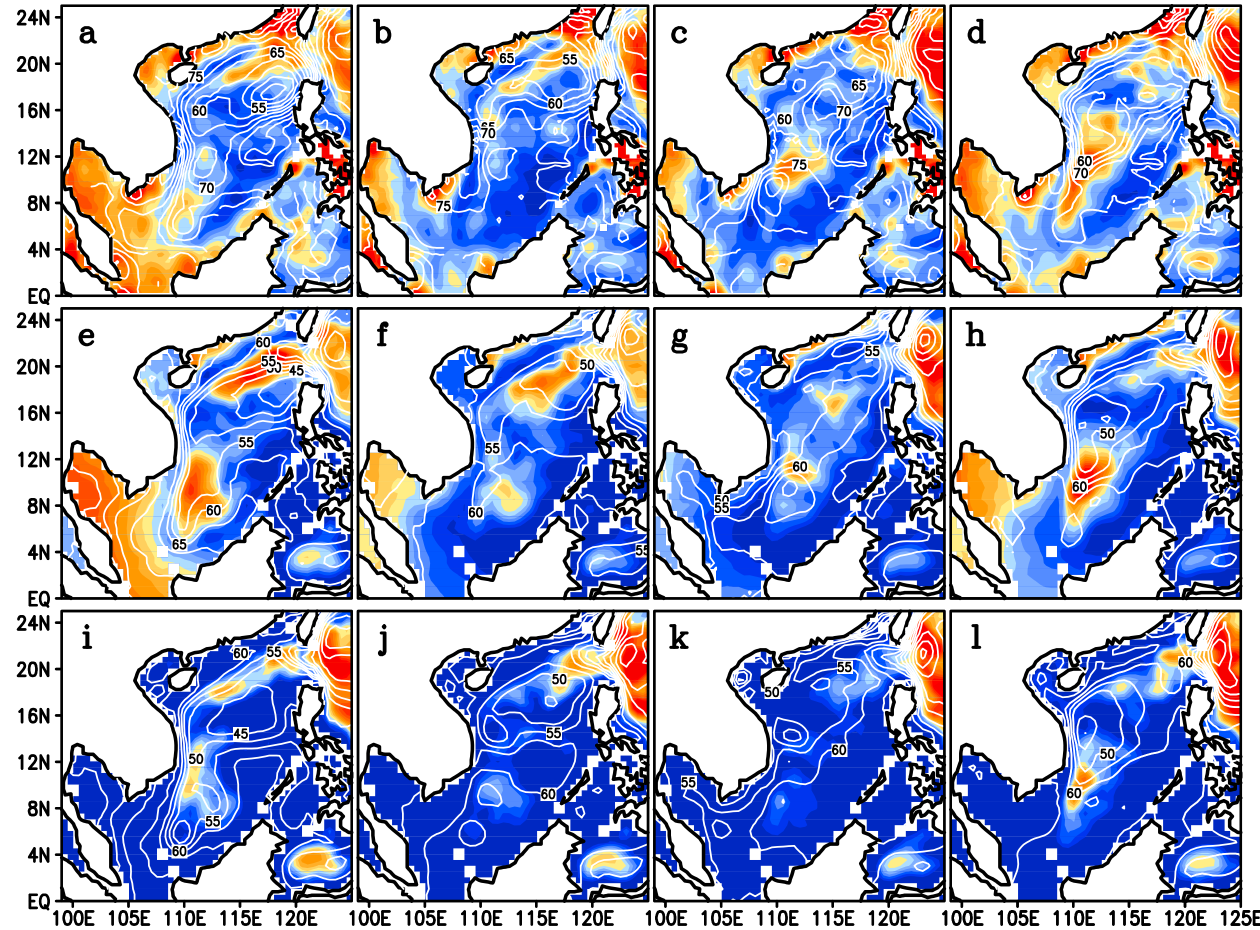

Figure 2. (a–d) The same as Figure 1a but for (a) winter, (b) spring, (c) summer, and (d) autumn; (e–h) the same as Figure 1b but for (e) winter, (f) spring, (g) summer, and (h) autumn; (i–l) the same as Figure 1c but for (i) winter, (j) spring, (k) summer, and (l) autumn.

southwest basins that separate high-variance bands in shallow and deep water regions (Figures 1a and 1b). Strikingly this low-variance band is roughly along the 150 m isobath, indicating that bottom topography could be an important factor for the spatial distribution of sea level ISV.

[20] SSH ISV in the SCS exhibits striking seasonality (Figure 2). In each season, the QSCAT run reproduces not only the observed mean but also the intraseasonal variance of SSH. The variance in the northern DW band west of Luzon Strait reaches its maximum in winter and minimum in summer. A similar seasonal trend is also found in the Gulf of Thailand. ISV on the NSCS shelf is strongest in autumn and weakest in spring, but its seasonality is relatively weak.

[21] The southern DW high-variance band becomes very active in autumn and remains so in winter. It runs in an approximately meridional direction. The maximum variance sits on the south flank of the basin-scale cyclonic circulation with large SSH gradient and strong current (Figures 2d and 2h). Not obvious in annual mean, there is a high-ISV region during summer east of southern Vietnam in both observations and QSCAT run, trapped apparently by the eastward offshore jet along 11–12°N (Figures 2c and 2g).

[22] Compared with the QSCAT run, ISV in the CLIM run is weak in the whole basin (Figure 1c). In shallow areas, the intraseasonal variance vanishes almost completely (<2 cm) throughout the year (Figures 2i–2l), suggesting the importance of high-frequency atmospheric forcing. In the deep basin, relatively high variance is still found west of Luzon Strait and southeast of Vietnam. In these DW high-variance bands, ISV displays the same seasonality as in observations and the QSCAT simulation, indicating that high-frequency atmospheric forcing is of secondary importance there.

3.2. Differences Between the Shelf and Deep Basin

[23] Results from the CLIM run indicate that SSH ISV is more sensitive to surface forcing on the shelf than in the deep basin. To further illustrate their difference, we select four locations, one in each of the above mentioned high-variance zones (see Figure 1a), and analyze the power spectra of observed SSH there. The annual and semiannual harmonics have been removed.

[24] The spectra are essentially red (Figure 3). In the subseasonal band, SSH is of higher frequencies on the NSCS shelf than in the northern DW band west of Luzon Strait (Figure 3a). Similarly, SSH in the Gulf of Thailand exhibits higher frequencies than in the southern DW band southeast of Vietnam (Figure 3b). The spectral power is higher in deep water for periods longer than 8 weeks while it

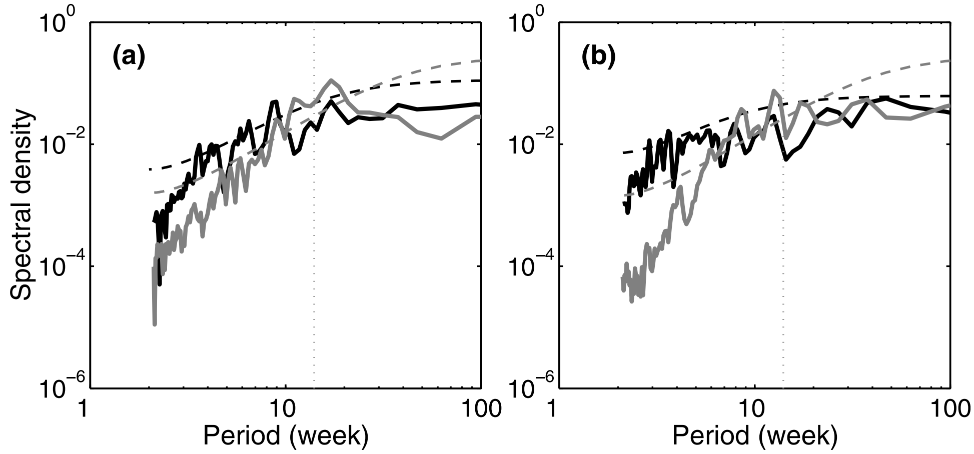

Figure 3. Comparison of power spectra between shallow (black line) and deep (gray line) zones, where the standard deviation of ISV is high for (a) observations on the NSCS shelf and to the south of the NSCS continental slope and (b) observations in the Gulf of Thailand and to the east of Vietnam coast. The positions selected for spectrum analysis are shown as black dots in Figure 1a. The 95% confidence levels are shown by dashed lines, and the dotted lines present the cutoff frequency for ISV signals.

is higher in shallow water at periods shorter than 6 weeks. Results from the QSCAT run are similar (not shown).

[25] To examine the contribution of density changes to SSH ISV, we calculate the steric height variations

$$\eta_{SH}(x,y,t) = -\frac{1}{\rho_0}\int_{-D}^{0}[\rho(x,y,z,t) - \rho_m(x,y,z)]dz,$$

where η is SSH anomaly, ρ is water density, ρ_m its time mean, and ρ_o a typical density. The bottom pressure contribution (η_b) to SSH can be derived as $\eta_b = \eta - \eta_{SH}$ [*Gill and Niiler*, 1973], due to the oceanic barotropic response to atmospheric forcing. Figure 4 presents intraseasonal variance of η_{SH} and η_b from the QSCAT run, revealing sharp contrasts between shallow and deep regions. In the deep basin, SSH ISV results from the density change in the water column, due to the baroclinic response to atmospheric forcing or ocean instability processes. On shallow shelves, sea level ISV is largely explained by barotropic adjustments to atmospheric forcing. In OFES, ocean barotropic motions are forced by surface wind stress and the barometric pressure effect is not considered. The latter is generally dynamically uninteresting and commonly removed from sea level records, such as altimeter data and tidal gauge measurements, by inverted barometer correction. Indeed, barotropic model experiments show that the dynamic ocean response to atmospheric pressure is much weaker than to wind forcing, especially in low-latitude coastal regions [*Carrère and Lyard*, 2003]. Therefore, observed ISV fluctuations in shallow waters of the SCS could be attributed to wind forcing and the approximation in OFES is reasonable for this work.

4. Origins of Intraseasonal Variability

[26] Owing to high resolution and accuracy of QuikScat wind, OFES captures spatial variations of SSH ISV quite well over the SCS. We take a further step to correlate observed and simulated SSH variability in time. Regions of high correlation indicate the importance of variable wind forcing while low correlations require additional consideration regarding the origin of ISV.

[27] Generally intraseasonal SSH correlation between observations and the OFES QSCAT simulation is higher in shelf regions than in the deep basin (Figure 5). Typical decorrelation timescale for ISV signals is about 6 weeks on the shelf and 10 weeks in the deep basin (not shown). For 7 year time series, the corresponding effective degrees of freedom for each season are around 15 and 9. Based on t test, the 95% significance level is 0.478 for the shelf and 0.592 for the deep basin correlation. In the Gulf of Thailand and the Sunda Shelf, the observation-OFES correlation mostly exceeds 0.5 in all seasons. Similar to variance shown in Figure 2, the observation-OFES correlation reaches a maximum in winter and minimum in summer.

[28] In the deep basin, the point to point correlation is generally low (Figure 5). The region along the offshore jet

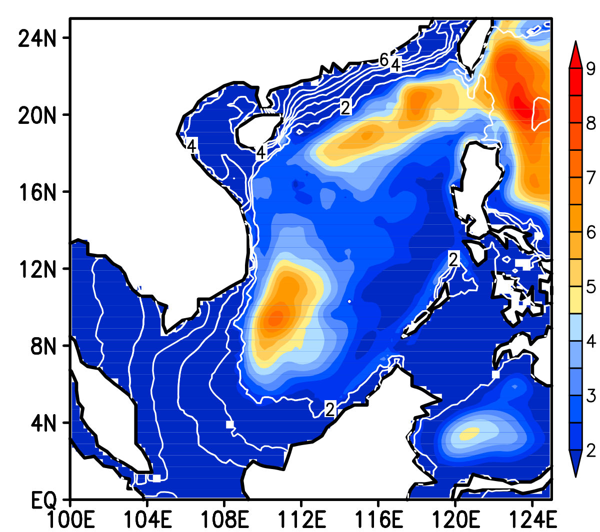

Figure 4. The intraseasonal variance of η_{SH} (cm, shaded areas) and $\eta - \eta_{SH}$ (cm, white contours).

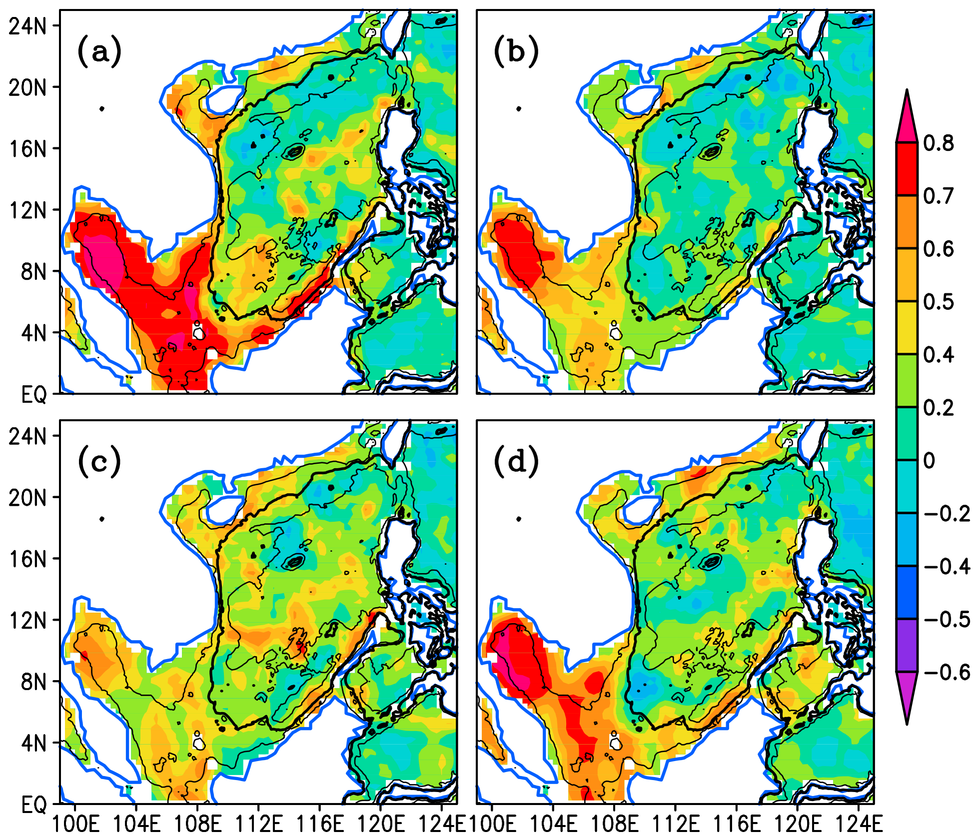

Figure 5. Point to point correlation coefficients between the intraseasonal SSH from altimetric observation and QSCAT run for (a) winter, (b) spring, (c) summer, and (d) autumn. The 50, 150, 2000 m isobaths are shown.

east of southern Vietnam (11°N) during summer is an exception, with correlation exceeding 0.6 (Figure 5c). High correlations also exist along the southeast boundary of the SCS basin, a region of small ISV variance. The high correlation there may be due to wind-forced coastal trapped Kelvin waves [*D. Wang et al.*, 2003]. Sections 4.1–4.4 investigate physical processes in high-variance zones identified above.

4.1. Gulf of Thailand and Other Shelf Regions

[29] SSH in the QSCAT simulation is highly correlated with observations in the Gulf of Thailand (Figure 5), especially in the interior around 101°E, 9°N. The correlation exceeds 0.8 during autumn to winter, 0.7 in spring and 0.6 in summer. Thus ISV is wind forced around the high-correlation center and influenced by other factors near the coast. The empirical orthogonal function (EOF) analysis is applied to examine spatial and temporal variations of ISV in the gulf. Figure 6 compares the first EOF mode (EOF-1) between the altimetric data and QSCAT run. The observed EOF-1 explains 52% of the total variance, with large amplitude at the high-correlation zone in Figure 5 and small amplitude near the coast and outside the gulf. The simulated EOF-1 accounts for 92% of the variance and is characterized by increasing amplitude from the mouth toward the head of the gulf. The simulated first principal component (PC-1) tracks the observed one remarkably well with a correlation coefficient of 0.84 (Figure 6c). The close agreement between observational and model PCs is consistent with high point correlation in Figure 5. Low amplitudes near the coasts in the observed EOF appear due to local tidal features. In the Gulf of Thailand, the diurnal and semidiurnal tides are both organized into rotary tidal waves, whose amplitudes are large around the coast and small near the amphidromes [*Mazzega and Bergé*, 1994, Figure 1]. Over continental shelves, tides are complex, and their modeling not yet satisfactory [*Lyard et al.*, 2006]. Strong tidal aliasing corrupts the altimeter data near the coast, and causes low correlation with OFES especially on the gulf head and the estuary of Mekong River, regions where the tidal amplitudes reach maxima (Figure 5). A similar problem exists in Taiwan Strait. Despite strong noise in coastal areas, the simulated EOF resembles observations in most of the gulf, indicating that atmospheric forcing is a dominant factor for SSH ISV.

[30] Figure 7a shows the regression of QuikScat wind vectors upon the observed PC-1 at lag 0. An intraseasonal fall of SSH in the gulf is associated with southwesterly wind anomalies. The lag correlation between a southwesterly wind ISV index and the PCs-1 reaches maximum of 0.57 and 0.73 at lag 0 for observation and QSCAT simulation, respectively (Figure 7b). With southwesterly (northeasterly) wind anomalies, SSH on the gulf head falls (rises) due to the outward (inward) Ekman transport and coastal waves. SSH anomalies are larger on the south than north coast of the Gulf (Figure 6b), indicative of a counterclockwise propagation of coastal Kelvin waves in response to the alongshore wind forcing on the northwest coast. The negative correla-

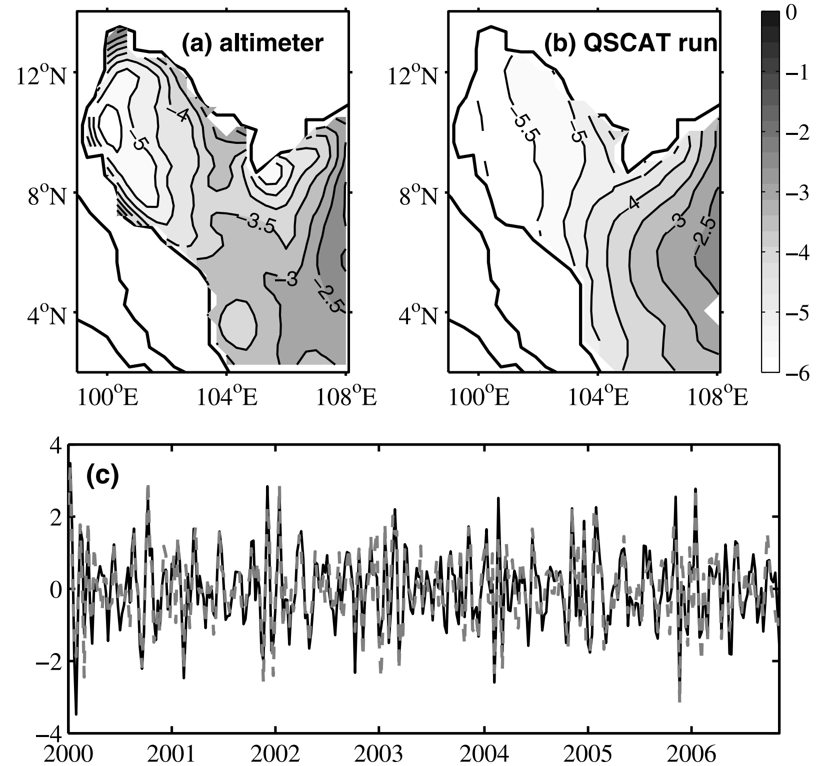

Figure 6. The first EOF of SSH intraseasonal signals in the Gulf of Thailand for (a) altimetric observation and (b) QSCAT run. (c) The first PCs of intraseasonal SSH for altimetric observation (solid line) and QSCAT run (dashed line).

tion between wind and observed SSH peaks at lags −2 and +3, suggesting a typical period of ISV around 35 days. The correlation at these lags is statistically insignificant, consistent with previous studies that ISV of the SCS monsoon does not have unique periods [e.g., *Annamalai and Slingo*, 2001].

[31] While the wind forcing plays a key role in SSH ISV in the gulf, the seasonality of intraseasonal SSH is not coincident with that of NE–SW wind ISV, which is weakest in summer but strongest in autumn. Figure 7c shows buoyancy frequency squared in the gulf based on density stratification from the QSCAT run. The simulated stratification in the gulf intensifies from spring to summer, remains strong in autumn, and vanishes in winter, consistent with previous hydrographic observations [*Yanagi et al.*, 2001]. The strong stratification reduces the barotropic response of sea level to wind forcing and weakens SSH ISV in shallow waters. In a barotropic Princeton Ocean Model simulation without ocean stratification, sea level ISV shows the same seasonality as wind ISV (not shown), suggesting the importance of seasonal stratification in modulating intraseasonal SSH.

[32] The sharp decrease in variance in the CLIM run suggests that SSH ISV on the NSCS shelf is also sensitive to high-frequency atmospheric forcing. Compared with the semienclosed Gulf of Thailand, the correlation on the NSCS shelf is mostly lower than 0.5 because of tidal aliasing in altimetry. Furthermore, the NSCS shelf is affected by complex dynamic processes such as coastal trapped waves through Taiwan Strait, the Kuroshio intrusion, and cross-shelf exchange. All these reduce model skills.

4.2. Along the Vietnam Offshore Jet During Summer

[33] The western SCS off the Vietnam coat is a dynamically active region. In summer, the southwesterlies are blocked by Annam Cordillera and accelerated to form a wind jet on the south edge of the mountain range [*Xie et al.*, 2003]. Numerical experiments by *Xu et al.* [2008] indicate that positive wind stress curls (WSCs) north of the wind jet is forced by the orographic blockage but negative WSCs to the south are part of large-scale atmospheric circulation rather than simply forced by orography. The resultant WSC dipole drives a double gyre in the ocean [*G. Wang et al.*, 2006; *Xu et al.*, 2008], with an eastward offshore jet on the intergyre boundary between 11°N and 12°N (Figures 2c and 2g). The ocean jet's separation from the coast involves a balance between wind stress and adverse pressure gradient force over shelf topography around the coastal promontory [*Gan and Qu*, 2008].

[34] On intraseasonal timescales, *Xie et al.* [2007] note that the double gyre circulation strengthens in 2 to 3 weeks in response to intraseasonal wind events via Rossby wave adjustment. High correlation (>0.6) with observations along the summer offshore jet (Figure 5) indicates that OFES captures this response to intraseasonal winds. We apply the EOF analysis to ISV during July–September (JJAS) in the southern SCS deep basin. EOF-1 patterns derived from observations and the QSCAT run both show strong loading in 11°N–12°N east of southern Vietnam (Figures 8a and 8b), representing the variability in the latitude of the offshore jet. The corresponding PCs-1 are highly correlated at 0.83. The PCs show 2–3 cycles for each summer season, with a typical

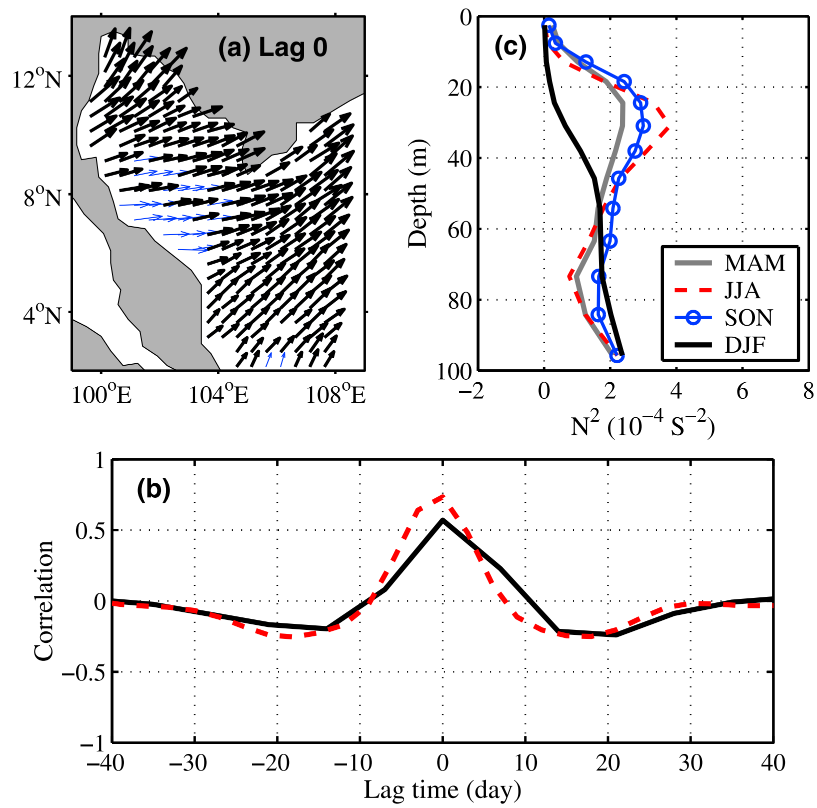

Figure 7. (a) Regression of sea surface wind (m/s, vectors) upon PC-1 of altimetric intraseasonal SSH. Thick vectors are between 99% confidence interval. (b) Lead-lag correlation coefficients between PCs-1 and a southwesterly wind index averaged in the Gulf of Thailand (solid line is for observational PC-1 and dashed line is for simulated PC-1). (c) Seasonal mean buoyancy frequency squared ($\times 10^{-4}$ s^{-2}) in the Gulf of Thailand.

period of 40–60 days. The explained variance (24% for observations and 31% for OFES) is relatively low, indicating that ISV is more complex than in the Gulf of Thailand. To validate the EOF analysis, we average SSH in a strip along the offshore jet where the standard deviation exceeds 5 cm (see Figure 2c). The PC-1 and this SSH index are correlated at 0.88 for observations, corroborating that the EOF mode well represents the summer ISV near the offshore jet.

[35] We apply the same EOF analysis to intraseasonal WSC during JJAS. The EOF-1 accounts for 40% of the total variance and exhibits a dipole structure with a stronger northern than southern pole (Figure 9a). Due to the latitudinal dependency of the Coriolis parameter, the intraseasonal Ekman Pumping velocity (w_e = $curl(\tau/f\rho)$) intensifies at lower latitudes and exhibits high variance with a maximum exceeding 5.5×10^{-6} m/s near the southern tip of Annam Cordillera. The meridional structure is suggestive of the blockage effect of the Annam range north of the wind jet. The PCs-1 for the summer modes of WSC and SSH are highly correlated. The maximum correlation (0.66) occurs when WSC leads observed SSH by 2 weeks (Figure 9b). OFES captures the lagged correlation curve very well, with a maximum of 0.63 occurring when WSC leads by 9 days. The lags for their correlations support the westward Rossby wave adjustment mechanism proposed by *Xie et al.* [2007]. We draw an analogy to the Kuroshio Extension, an inertial jet on the boundary between the subtropical and subpolar gyres. OFES achieves a similar success in capturing decadal variability of the inertial jet in response to basin-scale wind [*Taguchi et al.*, 2007]. At the latitude of the offshore jet, the critical period for first baroclinic Rossby waves is about 50–60 days (not shown) following *Lin et al.* [2008], while the jet may significantly modify the effective beta and critical period. With a typical period of 8 weeks, SSH ISV induced by the orographic wind jet features is permitted to travel westward as Rossby waves.

4.3. Northern DW Band

[36] Figure 10 shows the lag correlation of SSH ISV along the northern DW high-variance band west of Luzon Strait (Line 1 in Figure 1a). SSH at 117°E is taken as the reference time series. ISV displays a pronounced southwestward propagation during the active season of December–March (DJFM) but is somewhat localized during the inactive season of July–September (JJAS). During DJFM, typical oscillation period is 10–11 weeks, and typical phase speed is about 11 cm/s, consistent with eddy motions in the NSCS [*Wu and Chiang*, 2007]. The speed of eddy movement is comparable to both the current velocity averaged between 50 and 300 m along Line 1 and the phase speed of the first-mode baroclinic Rossby wave. Thus, the propagation of SSH variability along the northern DW band may represent eddy advection by mean flow or the signal of Rossby wave propagation. The correlation is weak in Luzon Strait, indicating that intraseasonal

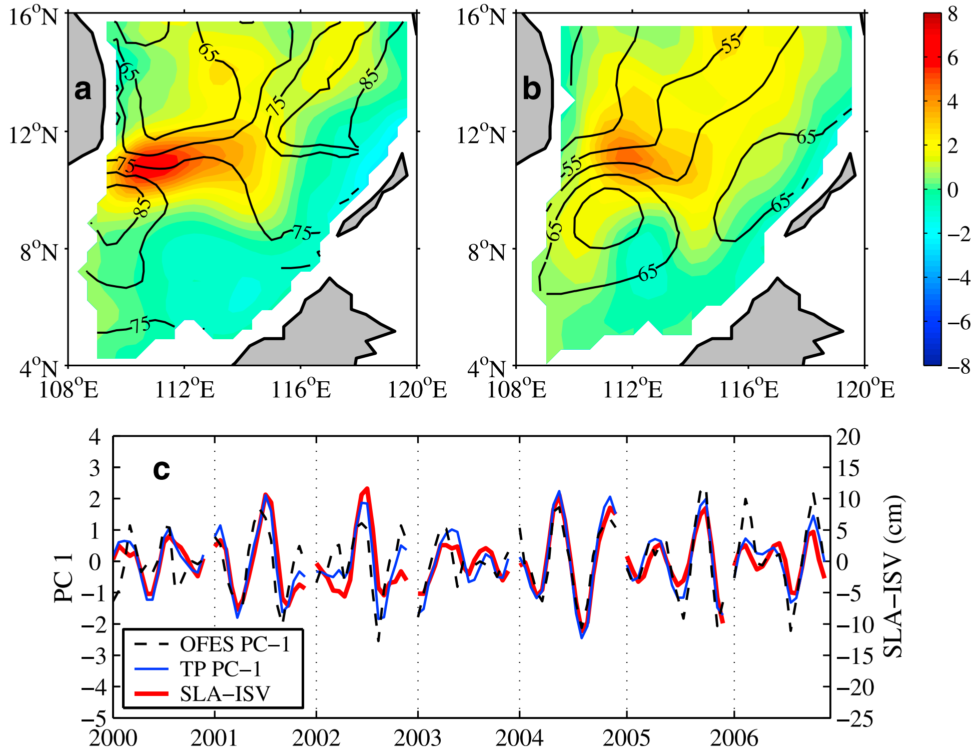

Figure 8. (a) EOF-1 of intraseasonal SSH in JJAS derived from altimeter observation (shaded areas), superimposed with observed mean SSH (black contours) during the same time. (b) EOF-1 of SSH ISV in JJAS derived from QSCAT run (shaded areas), superimposed with simulated mean SSH (black contour) during the same time. (c) PCs-1 of Figures 8a and 8b together with the time series of altimetric SSH ISV averaged at the region off Vietnam with standard deviation larger than 5 cm.

perturbations do not generally propagate directly from the western Pacific. Instead SSH ISV in the northern DW band is locally generated just west of Luzon Strait and then propagates southwestward, consistent with previous analyses [*Li et al.*, 2007; *Wu and Chiang*, 2007].

[37] The same lag correlation indicates that the QSCAT simulation captures the long-range, southwestward propagation in winter and rather stationary variability in summer along the northern DW band (not shown). The phase correlation between observations and OFES is low, suggestive of instability processes in deep waters. Energetics analysis elsewhere is useful to evaluate contributions from instabilities of mean flow and explain high SSH variability along the South Equatorial Current [e.g., *Feng and Wijffels*, 2002; *Yu and Potemra*, 2006]. Similar analysis has never been made in the SCS. We perform such an energetics analysis using the QSCAT simulation.

[38] Following *Böning and Budich* [1992], eddy kinetic energy (EKE) and eddy available potential energy (EPE) per unit mass are defined as follows:

$$EKE = \frac{1}{2}\left(u'^2 + v'^2\right),$$

$$EPE = -\frac{g\tilde{\rho}'^2}{2\rho(\partial\overline{\rho}_\theta/\partial z)},$$

where $\tilde{\rho}(x, y, z, t) = \rho(x, y, z, t) - \rho_b(z)$, $\rho_b(z)$ is a background density profile taken as the annual and horizontal mean within the SCS, and $\overline{\rho}_\theta(z)$ is the annual and horizontal mean potential density. Transient components of velocity and density are defined as variability of periods between 9 and 100 days and the residual low-frequency variations are treated as the basic state.

[39] The four-box energy diagram of *Lorenz* [1955] shows the energy transfer terms among various energy components. While the model output is not enough to close the mean and eddy energy budgets, some insights into instability mechanisms can be gained by considering energy transfers from mean to eddy energy. Specifically the conversion from mean to eddy potential energy, corresponding to baroclinic instability, is given by

$$T2 = -\frac{g}{\rho(\partial\overline{\rho}_\theta/\partial z)}\left(u'\tilde{\rho}'\frac{\partial\bar{\bar{\rho}}}{\partial x} + v'\tilde{\rho}'\frac{\partial\bar{\bar{\rho}}}{\partial y}\right).$$

The work of the Reynolds stresses against the mean shear is given by

$$T4 = -\left(u'u'\frac{\partial\bar{u}}{\partial x} + u'v'\left(\frac{\partial\bar{v}}{\partial x} + \frac{\partial\bar{u}}{\partial y}\right) + v'v'\frac{\partial\bar{v}}{\partial y}\right),$$

which if positive indicates the occurrence of barotropic instability.

[40] Since the flow and density fields are in quasi-geostrophic relationship in the SCS, the vertical integrated EKE and EPE show similar spatial patterns and seasonal cycles (not shown). So we use total eddy energy (TEE) as the sum of EKE and EPE. Figure 11 shows that there are

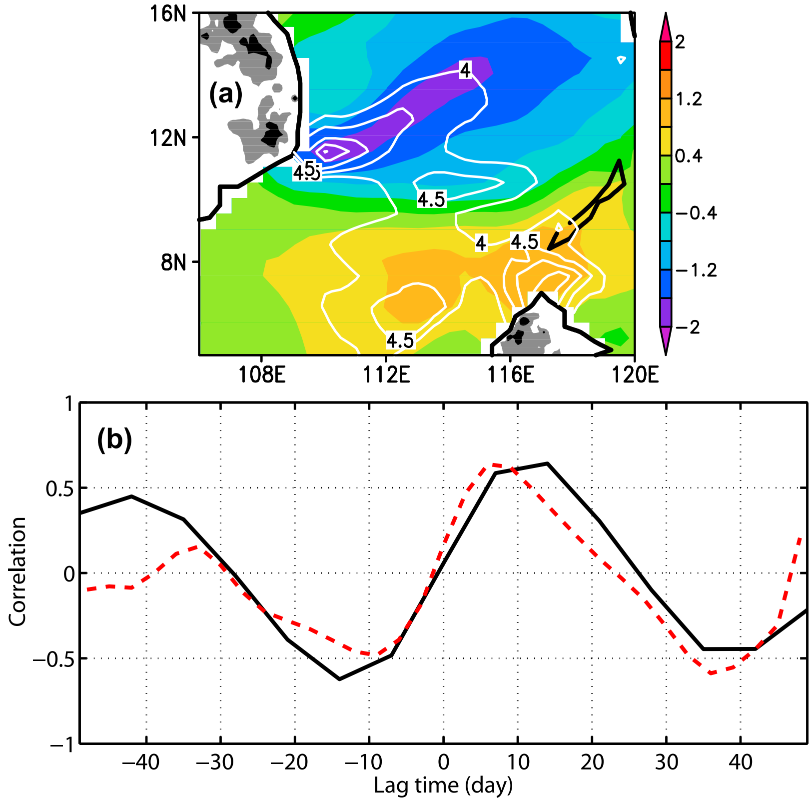

Figure 9. (a) EOF-1 of intraseasonal WSC (shaded areas), superimposed with standard deviation of intraseasonal Ekman pumping velocity (white contours, only the values >4 × 10^{-6} m/s are shown here) during the same time. (b) Lead-lag correlation coefficients of PCs-1 between WSC and SSH (solid line is for observed SSH and dashed line is for OFES SSH). Land orographies greater than 0.5 and 1 km are plotted in Figure 9a with gray and black shading.

two high-TEE zones, located west of Luzon Strait and southeast off Vietnam, consistent with the SSH variance distribution in deep waters. Figure 12 shows the seasonal cycle of eddy energy and the energy transfer terms in both DW band, averaged for 2000–2006 into a 5 day climatology. In both zones, TEE shows a similar seasonality to intraseasonal SSH variance. In shallow waters, TEE is small (<2 × 10^6 cm^3/s^2), in contrast to the SSH variance distribution.

[41] In the northern DW band, TEE maintains a high level around 15 × 10^6 cm^3/s^2 during January–February, decreases rapidly in March, and reaches a minimum value of about 4 × 10^6 cm^3/s^2 at the first pentad of August (Figure 12a). TEE increases slowly in September–October, and then rapidly in November–December. Baroclinic (T2) and barotropic (T4) conversions are both active but the former is stronger. The instabilities mainly occur in the eastern part of the high-TEE zone (Figure 11, white contours), consistent with Figure 10;

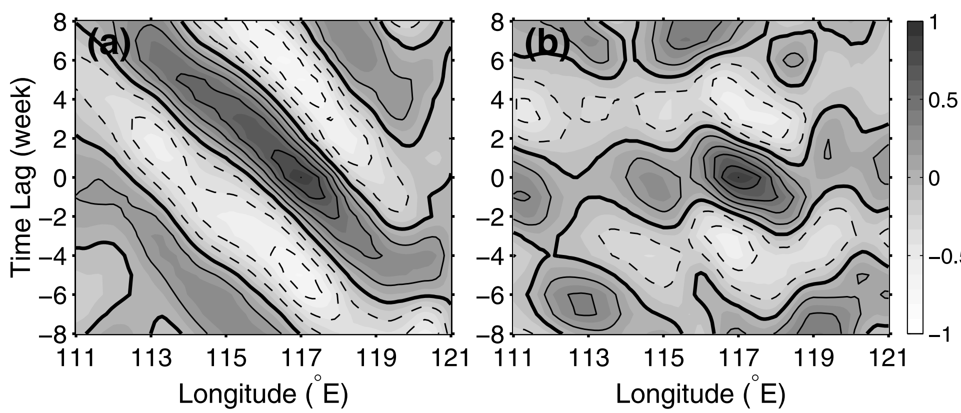

Figure 10. Time-longitude lag correlation of the observed intraseasonal SSH along Line 1 centered at 117°E (a) during December–March and (b) during June–September.

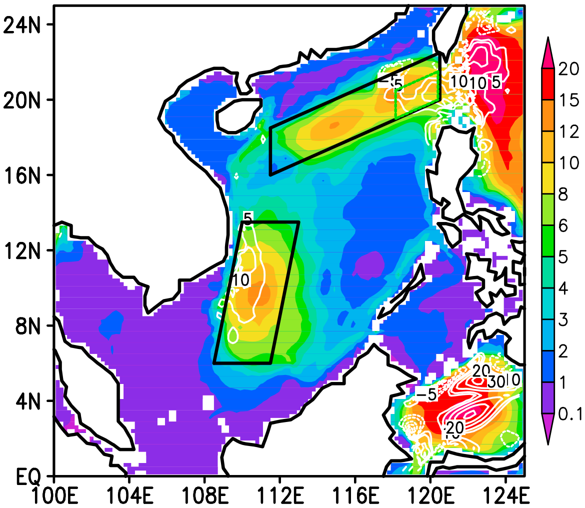

Figure 11. Annual mean vertical integrated TEE ($\times 10^6$ cm^3/s^2, shaded area) and the sum of T2 and T4 (cm^3/s^3, white contours).

TEE is generated near Luzon Strait by Kuroshio intrusion and then propagates southwestward following the mean flow or wave motion. As the area selected is large enough to cover active TEE, the instability term (T2+T4) dominates over the energy advection term ($\vec{v} \cdot \nabla TEE$) (Figure 12a), with the latter mainly affecting the spatial distribution of TEE within the high-variance zone. The sum of the instability and energy advection terms is in phase with TEE, suggesting a balance with dissipation that is presumably proportional to TEE, rather than with ∂TEE/∂t.

[42] Evolution of instabilities is affected by several factors, including the mean flow shear and ocean stratification. Here we take as an example the Kuroshio inflow zone west of Luzon Strait (green box in Figure 11), which is also the main instability zone within the northern DW band. Figure 13 shows the vertical velocity shear and stratification, both affecting the seasonal cycle of T2. The westward inflows and their vertical shears are both similar between autumn and winter, but T2 is much weaker in autumn because of stronger stratification and larger Richardson number in autumn. In summer, T2 is the weakest as the zonal velocity shear weakens and stratification strengthens.

4.4. Southern DW Band

[43] Figure 14 shows the latitude-lag sections of SSH correlation along the southern DW band (Line 2 in Figure 1a). SSH at 11°N is chosen as the reference time series. SSH variability displays a robust southward propagation during its active season of September–December (SOND) but is rather localized during the inactive season of March–June (MAMJ). During SOND, the typical oscillation period is about 8 weeks, and the phase speed about 19 cm/s in 9°N–13°N. The correlation in the southern DW band diminishes more quickly in distance than that in the northern DW band. During SOND, the southern DW band is located at the southwest corner of the basin-scale cyclonic circulation, and the southward-propagating, intraseasonal disturbances correspond to the variability in the southwest extent of this circulation.

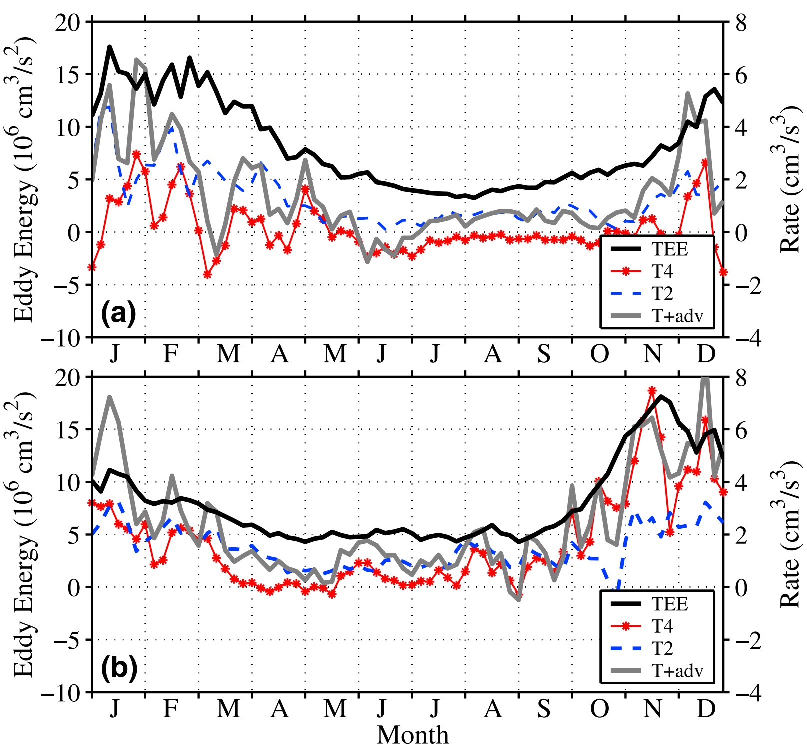

Figure 12. Five day climatology of mean TEE, T4, T2, and the sum of T4, T2, and TEE advection terms (T+adv) averaged in high-TEE boxes shown in Figure 11 (a) in the northern zone west of Luzon Strait and (b) in the southern zone southeast of Vietnam.

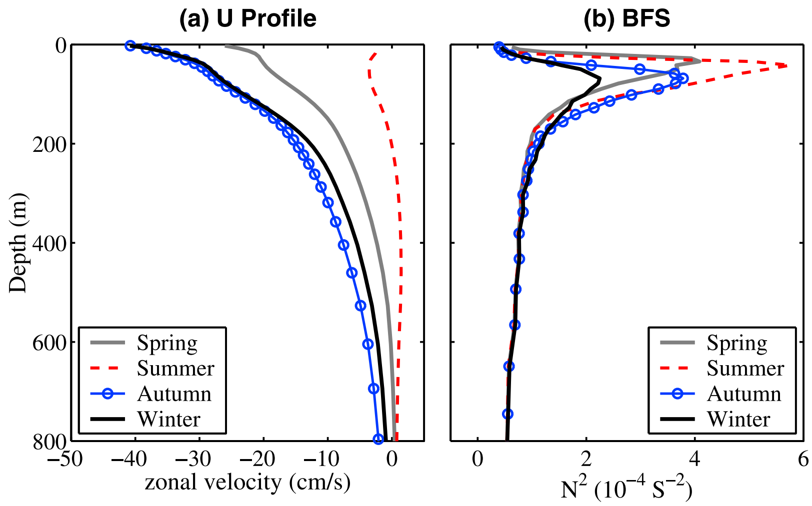

Figure 13. (a) Seasonal mean zonal velocity profile and (b) buoyancy frequency squared in the Kuroshio inflow area (averaged within the green box in Figure 11) from QSCAT run.

[44] In the southern DW band, TEE peaks at 18×10^6 cm^3/s^2 around the fifth pentad of November after a rapid increase during September and October (Figure 12b). TEE then falls from January and maintains low values around about 5×10^6 cm^3/s^2 during May–August. During high-TEE period, barotropic conversion T4 is much stronger than baroclinic conversion T2, different from most of the world ocean where baroclinic instability is the primary source of eddy energy [*Beckmann et al.*, 1994; *Stammer*, 1997]. The sum of instability and advection terms is in agreement with TEE rather than its time derivative, indicating the importance of dissipation as a sink of eddy energy.

5. Summary

[45] We have investigated SSH ISV in the SCS using the OFES hindcasts and satellite altimeter observations. SSH ISV is strong on the NSCS shelf, in the Gulf of Thailand, and in two deep water bands located south of the NSCS continental slope west of Luzon Strait and southeast off the Vietnam coast. The ISV shows evident seasonal variability. The standard deviation of intraseasonal SSH is high in the Gulf of Thailand during winter and in the NSCS shelf during autumn. In deep waters south of the NSCS continental slope, ISV is strongest in winter associated with marked southwestward propagations originating west of Luzon Strait. In the southern DW band southeast off Vietnam, ISV is strongest in autumn with southward propagation.

[46] ISV exhibits lower frequencies in deep than shallow water zones, suggesting distinct mechanisms between them. In the deep basin, SSH ISV is largely explained by steric height and associated with large, depth-integrated eddy energy. Both barotropic and baroclinic instabilities are important over both high-variance bands in deep waters. The sum of instability and energy advection terms is in phase with total eddy energy rather than its time derivative, suggesting the importance of dissipation as a sink of eddy energy. A quantitative estimation of the complete energy budget will be carried out in the future with more detailed modeling output. In summer, sea level ISV along the Vietnam offshore jet is well reproduced by the QSCAT simulation in both spatial pattern and temporal phase. Ocean Rossby waves may be important for the response to basin-scale, intraseasonal wind variability modulated by orographic effects of Annam Cordillera.

[47] ISV in shallow waters is dominated by the barotropic response to intraseasonal wind stress forcing. Over the Gulf of Thailand, the model reproduces observed SSH variability

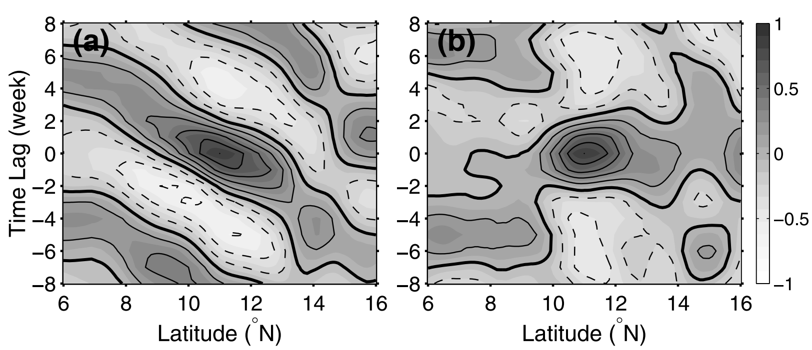

Figure 14. Time-latitude lag correlation of the observed intraseasonal SSH along Line 2 centered at 11°N (a) during September–December and (b) during March–June.

well, especially during winter when the density stratification is weak. In response to intraseasonal variations in the SCS monsoon, SSH in the Gulf rises and falls via Ekman transport and coastal waves. The counterclockwise propagation of coastal Kelvin waves, in particular, causes a stronger response in SSH on the southwest than the northeast coast of the Gulf in response to monsoon variability.

[48] High-SSH-variance regions in deep and shelf waters are separated by a low-variance band along 100–200 m isobaths. The ISV minimum along the continental break is consistent with our results that SSH variability on the shelves and in deep waters is produced by distinct mechanisms. The good agreement over the Gulf of Thailand between observations and the QSCAT simulation is somewhat surprising in light of the well-know aliasing errors due to strong tides in shelf waters. This result illustrates the utility of satellite altimetry over shelf regions of weak tides.

[49] **Acknowledgments.** We thank Xiaopei Lin and Yan Du for helpful suggestions on the paper. Comments by anonymous reviewers are highly appreciated. This work was supported by National Natural Science Foundation of China (grants 40806006, 40625017, 40830851, and 40876009), the Knowledge Innovation Project of the Chinese Academy of Sciences (KZCX2-YW-BR-04), the National Aeronautics and Space Administration, the National Science Foundation, and the Japan Agency for Marine-Earth Science and Technology. The work was initiated when W.Z. was a visiting student to the International Pacific Research Center (IPRC). IPRC/SOEST publication 658/7855.

References

Annamalai, H., and J. Slingo (2001), Acitve/break cycles: Diagnosis of the intraseasonal variability of the Asian summer monsoon, *Clim. Dyn.*, *18*, 85–102, doi:10.1007/s003820100161.

Beckmann, A., C. W. Boning, B. Brugge, and D. Stammer (1994), On the generation and role of eddy variability in the central North Atlantic Ocean, *J. Geophys. Res.*, *99*, 20,381–20,391, doi:10.1029/94JC01654.

Böning, C., and R. G. Budich (1992), Eddy dynamics in a primitive equation model: Sensitivity to horizontal resolution and friction, *J. Phys. Oceanogr.*, *22*, 361–381, doi:10.1175/1520-0485(1992)022<0361:EDIAPE>2.0.CO;2.

Boyer, T. P., and S. Levitus (1997), *Objective Analyses of Temperature and Salinity for the World Ocean on a 1/4° Grid*, *NOAA Atlas NESDIS*, vol. 11, NOAA, Silver Spring, Md.

Carrère, L., and F. Lyard (2003), Modeling the barotropic response of the global ocean to atmospheric wind and pressure forcing: Comparisons with observations, *Geophys. Res. Lett.*, *30*(6), 1275, doi:10.1029/2002GL016473.

Cheng, X., and Y. Qi (2007), Trends of sea level variations in the South China Sea from merged altimetry data, *Global Planet. Change*, *57*, 371–382, doi:10.1016/j.gloplacha.2007.01.005.

Chu, P. C., C. W. Fan, C. J. Lozano, and J. L. Kerling (1998), An airborne expendable bathythermograph survey of the South China Sea, May 1995, *J. Geophys. Res.*, *103*, 21,637–21,652, doi:10.1029/98JC02096.

Dale, W. (1956), Wind and drift current in the South China Sea, *Malays. J. Trop. Geogr.*, *8*, 1–31.

Dibarboure, G., O. Lauret, F. Mertz, V. Rosmorduc, and C. Maheu (2008), SSALTO/DUACS user handbook: (M)SLA and (M)ADT near-real time and delayed time products, *Rep. CLS-DOS-NT-06.034*, 39 pp., Aviso Altimetry, Ramonville St. Agne, France.

Fang, G., H. Chen, Z. Wei, Y. Wang, X. Wang, and C. Li (2006), Trends and interannual variability of the South China Sea surface winds, surface height, and surface temperature in the recent decade, *J. Geophys. Res.*, *111*, C11S16, doi:10.1029/2005JC003276.

Fang, W., G. Fang, P. Shi, Q. Huang, and Q. Xie (2002), Seasonal structures of upper layer circulation in the southern South China Sea from in situ observations, *J. Geophys. Res.*, *107*(C11), 3202, doi:10.1029/2002JC001343.

Feng, M., and S. Wijffels (2002), Intraseasonal variability in the South Equatorial Current of the east Indian Ocean, *J. Phys. Oceanogr.*, *32*, 265–277, doi:10.1175/1520-0485(2002)032<0265:IVITSE>2.0.CO;2.

Fukumori, I., R. Raghunath, and L. L. Fu (1998), Nature of the global large scale sea level variability in relation to atmospheric forcing: A modeling study, *J. Geophys. Res.*, *103*, 5493–5512, doi:10.1029/97JC02907.

Gan, J., and T. Qu (2008), Coastal jet separation and associated flow variability in the southwest South China Sea, *Deep Sea Res. Part I*, *55*, 1–19, doi:10.1016/j.dsr.2007.09.008.

Gan, J., H. Li, E. N. Curchitser, and D. B. Haidvogel (2006), Modeling South China Sea circulation: Response to seasonal forcing regimes, *J. Geophys. Res.*, *111*, C06034, doi:10.1029/2005JC003298.

Gao, R., and F. Zhou (2002), Monsoonal characteristics revealed by intraseasonal variability of sea surface temperature (SST) in the South China Sea (SCS), *Geophys. Res. Lett.*, *29*(8), 1222, doi:10.1029/2001GL014225.

Gill, A., and P. Niiler (1973), The theory of the seasonal variability in the ocean, *Deep Sea Res.*, *20*, 141–177.

Ho, C.-R., Q. Zheng, Y. S. Soong, N.-J. Kuo, and J.-H. Hu (2000a), Seasonal variability of sea surface height in the South China Sea observed with TOPEX/Poseidon altimeter data, *J. Geophys. Res.*, *105*(C6), 13,981–13,990, doi:10.1029/2000JC900001.

Ho, C.-R., N.-J. Kuo, Q. Zheng, and Y. S. Soong (2000b), Dynamically active areas in the South China Sea detected from TOPEX/Poseidon satellite altimeter data, *Remote Sens. Environ.*, *71*, 320–328, doi:10.1016/S0034-4257(99)00094-2.

Hwang, C., and S.-A. Chen (2000), Circulation and eddies over the South China Sea derived from TOPEX/Poseidon altimetry, *J. Geophys. Res.*, *105*(C10), 23,943–23,965, doi:10.1029/2000JC900092.

Kajikawa, Y., and T. Yasunari (2005), Interannual variability of the 10–25- and 30–60-day variation over the South China Sea during boreal summer, *Geophys. Res. Lett.*, *32*, L04710, doi:10.1029/2004GL021836.

Kalnay, E., et al. (1996), The NCEP/NCAR 40-year reanalysis project, *Bull. Am. Meteorol. Soc.*, *77*, 437–471, doi:10.1175/1520-0477(1996)077<0437:TNYRP>2.0.CO;2.

Lau, K. M., G. J. Yang, and S. H. Shen (1988), Seasonal and intraseasonal climatology of summer monsoon rainfall over East Asia, *Mon. Weather Rev.*, *116*, 18–37, doi:10.1175/1520-0493(1988)116<0018:SAICOS>2.0.CO;2.

Le Traon, P. Y., and G. Dibarboure (1999), Mesoscale mapping capabilities of multi-satellite altimeter missions, *J. Atmos. Oceanic Technol.*, *16*, 1208–1223, doi:10.1175/1520-0426(1999)016<1208:MMCOMS>2.0.CO;2.

Li, L., C. Jing, and D. Zhu (2007), Coupling and propagating of mesoscale sea level variability between the western Pacific and the South China Sea, *Chin. Sci. Bull.*, *52*(12), 1699–1707, doi:10.1007/s11434-007-0203-3.

Lin, X., J. Yang, D. Wu, and P. Zhai (2008), Explaining the global distribution of peak-spectrum variability of sea surface height, *Geophys. Res. Lett.*, *35*, L14602, doi:10.1029/2008GL034312.

Liu, Q., Y. Jia, P. Liu, and Q. Wang (2001), Seasonal and intraseasonal thermocline variability in the central South China Sea, *Geophys. Res. Lett.*, *28*(23), 4467–4470, doi:10.1029/2001GL013185.

Liu, Q., X. Jiang, S.-P. Xie, and W. T. Liu (2004), A gap in the Indo-Pacific warm pool over the South China Sea in boreal winter: Seasonal development and interannual variability, *J. Geophys. Res.*, *109*, C07012, doi:10.1029/2003JC002179.

Liu, W. T. (2002), Progress in scatterometer application, *J. Oceanogr.*, *58*, 121–136, doi:10.1023/A:1015832919110.

Liu, Z., H. Yang, and Q. Liu (2001), Regional dynamics of seasonal variability in the South China Sea, *J. Phys. Oceanogr.*, *31*, 272–284, doi:10.1175/1520-0485(2001)031<0272:RDOSVI>2.0.CO;2.

Lorenz, E. N. (1955), Available potential energy and the maintenance of the general circulation, *Tellus*, *7*, 157–167.

Lyard, F., F. Lefebre, and T. Letellier (2006), Modelling the global ocean tides: Modern insights from FES2004, *Ocean Dyn.*, *56*, 394–415.

Mao, J., and J. C. L. Chan (2005), Intraseasonal variability of the South China Sea summer monsoon, *J. Clim.*, *18*, 2388–2402, doi:10.1175/JCLI3395.1.

Masumoto, Y., et al. (2004), A fifty-year eddy-resolving simulation of the World Ocean—Preliminary outcomes of OFES (OGCM for the Earth Simulator), *J. Earth Simulator*, *1*, 31–52.

Maximenko, N. A., and P. P. Niiler (2005), Hybrid decade-mean global sea level with mesoscale resolution, in *Recent Advances in Marine Science and Technology 2004*, edited by N. Saxena, pp. 55–59, PACON, Honolulu.

Mazzega, P., and M. Bergé (1994), Ocean tides in the Asian semienclosed seas from TOPEX/POSEIDON, *J. Geophys. Res.*, *99*(C12), 24,867–24,881, doi:10.1029/94JC01756.

Metzger, E. J. (2003), Upper ocean sensitivity to wind forcing in the South China Sea, *J. Oceanogr.*, *59*, 783–798, doi:10.1023/B:JOCE.0000009570.41358.c5.

Metzger, E. J., and H. E. Hurlburt (2001), The nondeterministic nature of Kuroshio penetration and eddy shedding in the South China Sea, *J. Phys.*

Oceanogr., *31*, 1712–1732, doi:10.1175/1520-0485(2001)031<1712:TNNOKP>2.0.CO;2.

Pacanowski, R. C., and S. M. Griffies (2000), MOM 3.0 manual, technical report, 680 pp., Geophys. Fluid Dyn. Lab., Princeton, N. J.

Qiu, B. (1999), Seasonal eddy field modulation of the North Pacific subtropical countercurrent: TOPEX/Poseidon observations and theory, *J. Phys. Oceanogr.*, *29*, 2471–2486, doi:10.1175/1520-0485(1999)029<2471:SEFMOT>2.0.CO;2.

Qu, T. (2000), Upper-layer circulation in the South China Sea, *J. Phys. Oceanogr.*, *30*, 1450–1460, doi:10.1175/1520-0485(2000)030<1450:ULCITS>2.0.CO;2.

Qu, T., Y. Y. Kim, M. Yaremchuk, T. Tozuka, A. Ishida, and T. Yamagata (2004), Can Luzon Strait transport play a role in conveying the impact of ENSO to the South China Sea?, *J. Clim.*, *17*, 3644–3657, doi:10.1175/1520-0442(2004)017<3644:CLSTPA>2.0.CO;2.

Rong, Z., Y. Liu, H. Zong, and Y. Cheng (2007), Interannual sea level variability in the South China Sea and its response to ENSO, *Global Planet. Change*, *55*, 257–272, doi:10.1016/j.gloplacha.2006.08.001.

Sasaki, H., and M. Nonaka (2006), Far-reaching Hawaiian Lee countercurrent driven by wind-stress curl induced by warm SST band along the current, *Geophys. Res. Lett.*, *33*, L13602, doi:10.1029/2006GL026540.

Sasaki, H., Y. Sasai, S. Kawahara, M. Furuichi, F. Araki, A. Ishida, Y. Yamanaka, Y. Masumoto, and H. Sakuma (2004), A series of eddy resolving ocean simulations in the world ocean—OFES (OGCM for the Earth Simulator) project, paper presented at OCEANS 2004 Mar. Technol. Soc., Inst. of Electr. and Electr. Eng., Kobe, Japan.

Schlax, M. G., and D. B. Chelton (1994), Aliased tidal errors in TOPEX/Poseidon sea surface height data, *J. Geophys. Res.*, *99*, 24,761–24,775, doi:10.1029/94JC01925.

Shaw, P.-T. (1991), Seasonal variation of the intrusion of the Philippine Sea water into the South China Sea, *J. Geophys. Res.*, *96*, 821–827, doi:10.1029/90JC02367.

Shaw, P.-T., S. Y. Chao, and L. Fu (1999), Sea surface height variations in the South China Sea from satellite altimetry, *Oceanol. Acta*, *22*, 1–17, doi:10.1016/S0399-1784(99)80028-0.

Stammer, D. (1997), Global characteristics of ocean variability estimated from regional TOPEX/Poseidon altimeter measurements, *J. Phys. Oceanogr.*, *27*, 1743–1769, doi:10.1175/1520-0485(1997)027<1743:GCOOVE>2.0.CO;2.

Taguchi, B., S.-P. Xie, N. Schneider, M. Nonaka, H. Sasaki, and Y. Sasai (2007), Decadal variability of the Kuroshio Extension: Observations and an eddy-resolving model hindcast, *J. Clim.*, *20*, 2357–2377, doi:10.1175/JCLI4142.1.

Volkov, D. L., G. Larnicol, and J. Dorandeu (2007), Improving the quality of satellite altimetry data over continental shelves, *J. Geophys. Res.*, *112*, C06020, doi:10.1029/2006JC003765.

Wang, C., W. Wang, D. Wang, and Q. Wang (2006a), Interannual variability of the South China Sea associated with El Nino, *J. Geophys. Res.*, *111*, C03023, doi:10.1029/2005JC003333.

Wang, D., W. Wang, P. Shi, P. Guo, and Z. Gan (2003), Establishment and adjustment of monsoon-driven circulation in the South China Sea, *Sci. Chin. Ser. D*, *46*, 173–191, doi:10.1360/03yd9016.

Wang, G., J. Su, and P. C. Chu (2003), Mesoscale eddies in the South China Sea observed with altimeter data, *Geophys. Res. Lett.*, *30*(21), 2121, doi:10.1029/2003GL018532.

Wang, G., D. Chen, and J. Su (2006), Generation and life cycle of the dipole in the South China Sea summer circulation, *J. Geophys. Res.*, *111*, C06002, doi:10.1029/2005JC003314.

Wang, L. P., C. J. Koblinsky, and S. Howden (2000), Mesoscale variability in the South China Sea from the TOPEX/Poseidon altimetry data, *Deep Sea Res. Part I*, *47*, 681–708, doi:10.1016/S0967-0637(99)00068-0.

Wu, C.-R., and C.-W. J. Chang (2005), Interannual variability of the South China Sea in a data assimilation model, *Geophys. Res. Lett.*, *32*, L17611, doi:10.1029/2005GL023798.

Wu, C.-R., and T.-L. Chiang (2007), Mesoscale eddies in the northern South China Sea, *Deep Sea Res. Part II*, *54*, 1575–1588, doi:10.1016/j.dsr2.2007.05.008.

Wu, C.-R., T. Y. Tang, and S. F. Lin (2005), Intra-seasonal variation in the velocity field of the northeastern South China Sea, *Cont. Shelf Res.*, *25*, 2075–2083, doi:10.1016/j.csr.2005.03.005.

Wyrtki, K. (1961), Physical oceanography of the southeast Asian waters: Scientific results of marine investigations of the South China Sea and the Gulf of Thailand, *NAGA Rep. 2*, 195 pp., Scripps Inst. of Oceanogr, La Jolla, Calif.

Xie, S.-P., Q. Xie, D. Wang, and W. T. Liu (2003), Summer upwelling in the South China Sea and its role in regional climate variations, *J. Geophys. Res.*, *108*(C8), 3261, doi:10.1029/2003JC001867.

Xie, S.-P., C.-H. Chang, Q. Xie, and D. Wang (2007), Intraseasonal variability in the summer South China Sea: Wind jet, cold filament, and recirculations, *J. Geophys. Res.*, *112*, C10008, doi:10.1029/2007JC004238.

Xiu, P. F. Chai, L. Shi, H. Xue, and Y. Chao (2010), A census of eddy activities in the South China Sea during 1993–2007, *J. Geophys. Res.*, *115*, C03012, doi:10.1029/2009JC005657.

Xu, H., S.-P. Xie, Y. Wang, W. Zhuang, and D. Wang (2008), Orographic effects on South China Sea summer climate, *Meteorol. Atmos. Phys.*, *100*, 275–289, doi:10.1007/s00703-008-0309-4.

Xu, X. Z., Z. Qiu, and H. C. Chen (1982), The general descriptions of the horizontal circulation in the South China Sea (in Chinese with English abstract), in *Proceedings of the 1980 Symposium on Hydrometeorology of the Chinese Society of Oceanology and Limnology*, edited by Editorial Board of Oceanology and Limnology Society, pp. 137–145, Sci. Press, Beijing.

Yanagi, T., S. Sachoemar, T. Takao, and S. Fujiwara (2001), Seasonal variation of stratification in the Gulf of Thailand, *J. Oceanogr.*, *57*, 461–470, doi:10.1023/A:1021237721368.

Yu, Z., and J. Potemra (2006), Generation mechanism for the intraseasonal variability in the Indo-Australian basin, *J. Geophys. Res.*, *111*, C01013, doi:10.1029/2005JC003023.

Yuan, D., W. Han, and D. Hu (2006), Surface Kuroshio path in the Luzon Strait area derived from satellite remote sensing data, *J. Geophys. Res.*, *111*, C11007, doi:10.1029/2005JC003412.

H. Aiki, H. Sasaki, and B. Taguchi, Earth Simulator Center, Japan Agency for Marine-Earth Science and Technology, 3173-25 Showa-machi, Kanazawa-ku, Yokohama 236-0001, Japan.

D. Wang and W. Zhuang, Key Laboratory of Tropical Marine Environmental Dynamics, South China Sea Institute of Oceanology, 164 West Xingang Rd., Guangzhou 510301, China. (zhuang@scsio.ac.cn)

S.-P. Xie, International Pacific Research Center, University of Hawai'i at Manoa, 1680 East-West Rd., Honolulu, HI 96822, USA.